Physica Scripta

PAPER • OPEN ACCESS

Analysis of anode surface roughness influence on heaterless hollow cathode discharge

To cite this article: Jordan H Hsieh *et al* 2024 *Phys. Scr.* **99** 035607

IOP Publishing Phys. Scr. 99 (2024) 035607 https://doi.org/10.1088/1402-4896/ad24a7

Physica Scripta

RECEIVED
6 October 2023

REVISED
21 November 2023

ACCEPTED FOR PUBLICATION
31 January 2024

PUBLISHED
15 February 2024

PAPER

Analysis of anode surface roughness influence on heaterless hollow cathode discharge

Jordan H Hsieh[1], **Ping-Han Huang**[1], **Yi-Lung Huang**[1], **Heri Juwantono**[2] **and Yueh-Heng Li**[1,2]

[1] Department of Aeronautics and Astronautics, National Cheng Kung University, Tainan, 70101, Taiwan
[2] International Doctoral Degree Program on Energy Engineering, National Cheng Kung University, Tainan, 70101, Taiwan

E-mail: yueheng@mail.ncku.edu.tw **and** yuehheng.li@gmail.com

Keywords: cathode, heaterless, roughness, anode, discharge

Abstract

This research delves into the influence of cylindrical and planar anode surface roughness on heaterless hollow cathode discharge characteristics. Three surface roughness levels, Ra 1.6 μm, Ra 3.2 μm, and Ra 6.4 μm, along the cylindrical anode's azimuthal direction and the planar anode's radial direction, have been selected and modified by the machining process. A central finding is the correlation between the discharge voltage and anode surface roughness. As the roughness increases, cylindrical and planar anodes require less discharge voltage to sustain the primary discharge. This reduction is likely due to the enhanced surface area from the roughness, which aids in electron current collection. The discharge voltage oscillations appear inversely related to the surface roughness of planar anodes, which may be associated with changes in the neutral gas density gradient between the planar anode and the cathode. In contrast, cylindrical anodes show fewer effects from their surface roughness, likely due to the distinct neutral gas flow dynamics. These findings offer insights into standardizing hollow cathode testing and allow future research to explore these interactions more deeply.

1. Introduction

The genesis of electric propulsion can be traced back to the early 1900s when Russian scientist Konstantin Tsiolkovsky proposed generating thrust from electrically charged particles [1]. Since that pioneering proposition, electric propulsion has seen accelerated advancements and has been integrated into satellite missions [2, 3]. When categorized from the perspective of plasma discharge, electric propulsion can be broadly classified into pulsed plasma propulsion and steady-state plasma thrusters. Pulsed plasma propulsion, exemplified by pulsed plasma thrusters and vacuum arc thrusters [4–6], operates on intermittent firings that cumulatively achieve a specific impulse. In contrast, steady-state electric thruster, represented by ion and Hall thrusters [7–12], maintains continuous firing over determined durations. Notably, hollow cathodes utilize thermionic emission and serve dual roles in steady-state plasma thrusters, acting as neutralizers for the outgoing ion beam and as electron sources for propellant ionization [13].

Hollow cathodes typically consist of four primary components: emitter, cathode tube, keeper, and heater. The emitter, or insert, is often crafted from low work function materials [14]. This design ensures sufficient thermionic emission current below the melting points of the material itself and its supporting material. The journey of discovering suitable emitter materials for hollow cathodes dates back to the early 20th century, marking the inception of the first cathode [15]. Initial hollow cathodes utilized oxide layers deposited on metal filaments, such as tungsten and nickel, to serve as the emitter material [16]. However, these oxide surface layers presented challenges; they could be readily sputtered by ion bombardment, which curtailed their operational lifespan [16]. Therefore, dispenser cathodes were developed to address this issue by continuously replenishing the low work function surface layer [17, 18]. This innovation allowed higher emission current densities and extended lifetimes compared to oxide-coated cathodes [19].

Nevertheless, dispenser cathodes encountered their issues; forming the low work function surface often inadvertently increased the emitter's work function due to chemical reactions [20]. This led to the rise of lanthanum hexaboride, a refractory compound characterized by its low work function, high melting point, and robust chemical stability, making it an ideal choice for cathode applications, particularly in satellite missions [21–23]. Calcium aluminate electride (C12A7) is a promising contender for future electric propulsion endeavors [24, 25]. While the exact work function of C12A7 remains a topic of debate, there is a consensus in the academic community that C12A7 boasts a notably lower work function compared to traditional emitter materials [16].

The cathode tube, which houses the fixed emitter, serves as the primary structural body of the cathode. Choosing materials for the cathode tube demands careful consideration. These materials must possess high melting points, such as refractory metals or graphite, and maintain exceptional chemical stability at elevated temperatures [26, 27]. This stability is essential to prevent any chemical reactions with the emitter material, which could escalate the emitter's work function, increasing discharge voltage. Such changes could adversely affect the performance of the hollow cathode [13].

Refractory metals present challenges in designs involving lanthanum hexaboride hollow cathodes. Under high temperatures, most refractory metals react chemically with lanthanum hexaboride [28]. The boron from lanthanum hexaboride is prone to diffuse into the supporting structure of the refractory metal at high temperatures, which not only heightens the work function of the lanthanum hexaboride but also results in the embrittlement of the refractory metal [14]. Consequently, when refractory metals are selected as the material for the cathode tube, a thin graphite sheath is typically employed to cover the exterior of the emitter, ensuring no direct contact between it and the cathode tube [29].

The keeper of a hollow cathode plays a pivotal role in managing the cathode's temperature and can also serve as the ignitor for the hollow cathode [13]. In heaterless hollow cathodes, the discharge between the keeper and the cathode tube assists in heating the emitter [30]. Furthermore, the keeper acts as a protective shield for the cathode tube and the emitter, preventing them from high-energy ion bombardment originating from the plume region [31].

In hollow cathodes, the function of the heater is to pre-heat the emitter to its thermionic temperature, sufficient for establishing the primary discharge with the anode before hollow cathode operation commences. Classical hollow cathode designs frequently employ tantalum-sheathed alumina-insulated heaters wrapped around the cathode tube [27, 32]. Given the risks associated with external heaters, such as thermal fatigue and the potential for short-circuiting with metallic foils or the cathode tube [14], there has been a growing interest in heaterless hollow cathodes in recent years [30]. This design approach mitigates cathode failure risks by eliminating the need for external heaters. In this setup, the emitter is heated to its thermionic temperature through plasma discharge. Once the emitter reaches its working temperature, it can sustain the discharge with the anode [33]. This heaterless approach presents several advantages. Firstly, it eliminates the heater, which is prone to damage from repetitive heating-induced thermal fatigue [32]. Secondly, plasma heating can expedite the cathode ignition process [34]. As the cathode tube and emitter are directly heated by plasma discharge instead of indirect heating from an external heater, this significantly speeds up the time required to heat the emitter to its thermionic temperature, reducing the warming process from several minutes to mere seconds [34].

The anode, the electrode directly involved with cathode discharge, can potentially influence hollow cathode discharge characteristics based on its geometry, size, distance from the cathode, and material composition. While most research on cathodes primarily focuses on prolonging their lifespan and understanding the causes of discharge instabilities [35, 36], there is a noticeable gap in examining the impact of cathode test equipment on its discharge characteristics. Moreover, the variability in experimental setups, such as different power supplies, vacuum chambers, and procedures used in existing research, makes it challenging to analyze the effects of facilities on cathode operation quantitatively.

Although a few studies have previously documented the impact of experimental design and test equipment on hollow cathode discharge characteristics, including the effects of anode position [30, 37, 38] and geometry [39–42] on cathode discharge profiles and plumes. Given the under-explored theme of anode surface roughness and its influence on hollow cathode discharge, this study will investigate the impact of the surface roughness of cylinder and planar anode on cathode operation characteristics, aiming to lay a foundational basis for standardizing future hollow cathode testing.

This research investigates the discharge characteristics of heaterless hollow cathodes, focusing on three distinct aspects. Initially, the study evaluates the discharge voltage and its oscillations under operational conditions involving both cylinder and planar anodes, with discharge currents ranging from 4 A to 6 A and gas flow rates between 9 sccm and 11 sccm. Subsequently, the influence of surface roughness on the discharge voltage for both cylindrical and planar anodes is assessed, bearing in mind the expected effect due to the direct correlation between surface roughness and surface area. Finally, the investigation examines the ramifications of anode surface roughness on ionization-like instabilities and ion-acoustic turbulence (IAT) within the cathode plume, harnessing power spectral density (PSD) analysis to investigate these phenomena comprehensively.

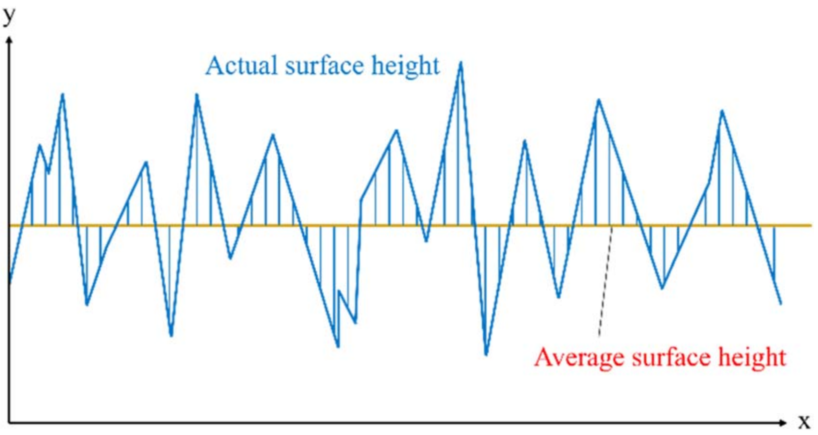

Figure 1. Comparison of actual surface height and average surface height.

2. Anode design

2.1. Surface roughness

Surface roughness is a parameter that describes the minute irregularities on an object's surface, which may arise from manufacturing processes, material properties, or other external factors. Average roughness, denoted as Ra, stands out as a commonly used parameter. Ra represents the average deviation between the surface roughness curve and its baseline. This parameter finds applications in mechanical engineering, manufacturing, and several other fields. Surface roughness is intrinsically linked to properties such as friction, sealing capability, and the appearance of a component [43]. Mathematically, the average roughness, Ra, is typically defined as the average of the absolute values of these minute irregularities over a specified length. Specifically, given a surface height function $y(x)$, Ra over a length L can be represented as [44]:

$$\mathrm{R_a} = \frac{1}{L}\int_0^L |y(x) - y_{avg}|\ dx, \tag{1}$$

where y_{avg} denotes the average surface height. Figure 1 compares the actual surface height post-mechanical processing and the average height of the surface. In this study, to represent the surface roughness of both cylindrical and planar anodes, three levels of surface roughness were selected: Ra 1.6 μm, Ra 3.2 μm, and Ra 6.4 μm, measured along the azimuthal direction of the cylindrical anode and the radial direction of the planar anode.

2.2. Anode geometry

The anode serves as the electrode for establishing a primary discharge with the cathode and influences the discharge characteristics of the hollow cathode through its geometry, dimension, and distance between itself and the cathode. Based on existing studies, table 1 summarizes an overview of anode materials, geometry, dimensions, and the distance from the cathode. 'O.D.' in table 1 denotes the outside diameter, while 'I.D.' signifies the inside diameter. It is observed that existing studies primarily utilized four primary anode materials: stainless steel (mainly of the non-magnetic variety), graphite, molybdenum, and copper. The anodes are mostly cylindrical or disk-shaped geometries, with many researchers perforating the disks to mitigate the excessive accumulation of neutral gas density between them and the cathode. Furthermore, the typical anode-to-cathode distance spans between 20 to 200 mm.

Based on the information compiled in table 1, this study utilizes cylindrical and planar anode geometries to investigate the impact of anode surface roughness on cathode discharge. Figure 2 provides the schematics of the two anodes in use. Figure 2(a) displays a cylinder with an inside diameter of 70 mm, an outside diameter of 80 mm, and a length of 100 mm. In contrast, figure 2(b) illustrates a planar anode with a diameter of 100 mm and a thickness of 5 mm. Both anodes are fabricated from non-magnetic stainless steel.

The design of the cylindrical anode consists of two half-cylinders secured together using four screws. This construction was chosen to facilitate mechanical processing on the inner surface of the cylinder, allowing for the creation of varying surface roughness levels. The planar anode features seven holes, each with a diameter of 5 mm, distributed around its center. These holes are designed to prevent excessive accumulation of neutral gas between the anode and the cathode. Additionally, a rectangular protrusion on the right side of the planar anode serves as a supporting structure, anchoring the anode to the vacuum chamber.

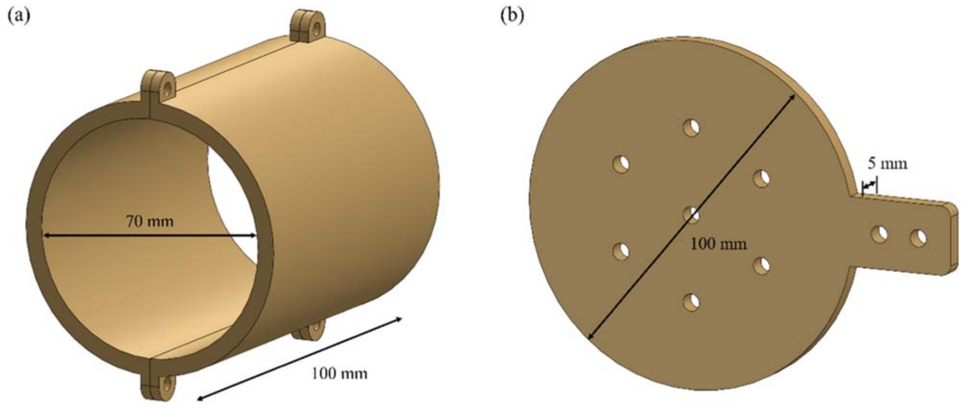

Figure 2. Schematics of the utilized (a) cylindrical anode and (b) planar anode.

Table 1. Summary of anode characteristics from existing studies.

Researcher	Material	Geometry	Dimension	Distance
Joussot *et al* [45]	Stainless steel	Annular plate	O.D. of 210 mm, I.D. of 21 mm	20 mm
Coletti and Gabriel [46]	Graphite	Apertured disk		40, 100 mm
Brophy and Garner [47]	Copper	Cylinder and disk	I.D. of 213 mm for the cylinder, O.D. of 150 mm for the disk	120 mm
Brophy and Garner [48]	Molybdenum	Disk		130 mm
Kamhawi and Van-Noord [49]	Molybdenum	Cylinder	Diameter of 200 mm	200 mm
Puchkov [50]		Perforated plate	Holes 6.5 mm in diameter	6 mm
Goebel and Polk [51]	Copper	Cylinder		
Oshio *et al* [52]	Graphite	Ring	O.D. of 100 mm, I.D. of 50 mm	37 mm
Ning *et al* [53]	Molybdenum	Plate	100 mm × 100 mm × 2 mm	20 mm
Drobny *et al* [54]	Copper	Cylinder	Diameter of 100 mm	100 mm
Vekselman *et al* [33]	Stainless steel	Plate	Thickness of 2 mm, I.D. of 1 mm	20, 30 mm
Chu and Goebel [55]	Copper	Two cylinders		
Potrivitu *et al* [37]	Stainless steel	Disk	O.D. of 110 mm	20–70 mm
Lev *et al* [56]	Stainless steel	Plate		40 mm
Potrivitu *et al* [39]	Stainless steel	Plate	Surface area of 411.3 cm^2	20 mm
	Stainless steel	Disk	O.D. of 110 mm	20 mm
	Stainless steel	Long cylinder	I.D. of 111.3 mm, length of 117.6 mm	20 mm
	Stainless steel	Short cylinder	I.D. of 111.3 mm, length of 27.8 mm	20 mm

2.3. Surface area

Surface roughness is typically influenced by the method of machining. In this study, to maintain consistency in anode surface conditions, anodes with three different levels of surface roughness were fabricated using computer numerical control (CNC) machining, with adjustments to the CNC machine settings to achieve the desired roughness. The surface areas of the anodes were estimated under ideal manufacturing conditions. The CNC machining tool follows an axial feed path for cylindrical anodes, while it follows an azimuthal path for planar anodes. Assuming that the machining of the anode surfaces meets the ideal state defined by surface roughness Ra, the roughness along the cylindrical anode's axial direction and the planar anode's azimuthal direction are presumed to be Ra 0 μm.

In contrast, the roughness in the cylindrical anode's azimuthal direction and the planar anode's radial direction is set at Ra 1.6 μm, Ra 3.2 μm, and Ra 6.4 μm. The surface areas corresponding to these roughness levels were calculated, assuming that the tooling marks on the anode surfaces create isosceles triangles with bases measuring 1 μm and heights of 3.2 μm, 6.4 μm, and 12.8 μm. These calculations enabled the determination of the surface areas of both cylindrical and planar anodes under ideal conditions, as illustrated in figure 3.

It should be noted that the Ra values of 1.6 μm, 3.2 μm, and 6.4 μm in cylindrical and planar anodes correspond to the azimuthal and radial directions, respectively. Additionally, since the surface roughness along the axial and azimuthal directions of the cylindrical and planar anodes is assumed to be Ra 0 μm, the actual anode surface roughness Ra will be less than 1.6 μm, 3.2 μm, and 6.4 μm. However, for clarity in this study, the

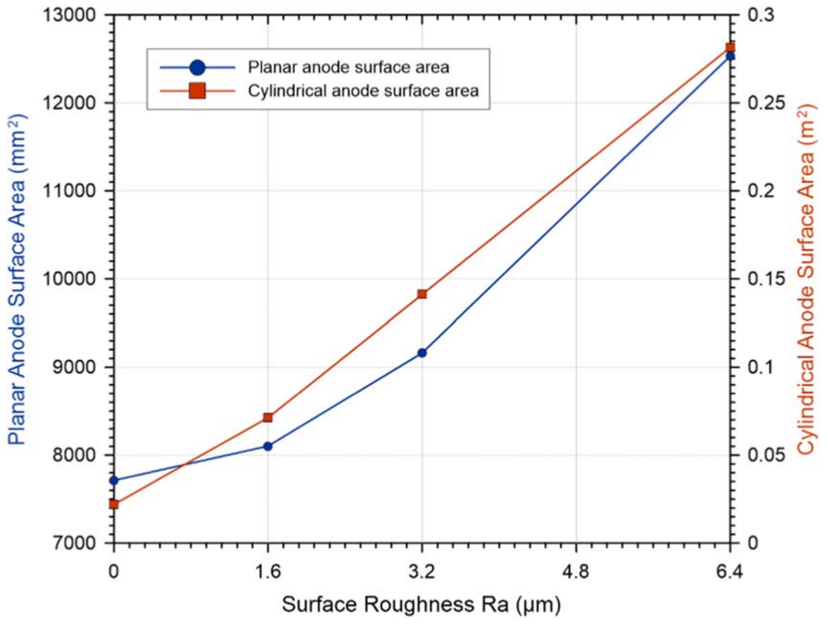

Figure 3. Surface area variation of cylindrical and planar anodes with different surface roughness values.

terms Ra 1.6 μm, Ra 3.2 μm, and Ra 6.4 μm are used directly to refer to anodes with different surface roughness levels.

3. Experimental design

3.1. Heaterless hollow cathode

Hollow cathodes can be categorized based on the diameter of their cathode tube orifice into two main types: open-end emitter cathodes and orificed emitter cathodes. The former lacks a distinct cathode tube orifice, and its opening typically aligns closely with the emitter's inner diameter. The design adopted in this study corresponds to the latter, the orifice cathode, meaning that the orifice at the forefront of the cathode tube aids in augmenting the neutral gas density within the cathode tube. The diameter of the cathode tube orifice plays a pivotal role, as varying diameters will potentially alter the self-heating mechanism of hollow cathodes.

Self-heating in hollow cathodes refers to the intrinsic mechanism whereby the emitter is maintained at its thermionic temperature during discharge through plasma bombardment. When operating in a self-heating mode, the hollow cathode's primary sources of heating derive from electron and ion bombardment in both the insert and orifice regions, as well as orifice heating [13].

In the design of an orifice cathode, the gas pressure inside the cathode is heightened due to the presence of the orifice. This elevation in pressure amplifies the kinetic energy electrons deposit on the emitter surface during the bombardment, resulting from reduced electron temperatures and sheath potentials [13]. Simultaneously, ion bombardment in the orifice cathode decreases because of these diminished sheath potentials [14].

Orifice heating also experiences an enhancement due to the small aperture of the cathode tube. As the plasma maneuvers through the orifice, it faces significant resistance, manifesting as increased collisions between charged particles, generating notable resistive heating in the orifice plasma. This action elevates the temperature of the orifice plate, which heats the emitter eventually. Figure 4 is the photograph of the hollow cathode used in this study after 25 h of discharge.

Figure 5 depicts the cross-sectional view of the heaterless hollow cathode. The emitter of this cathode is made of press-sintered lanthanum hexaboride with an inner diameter of 3 mm, an outer diameter of 5 mm, and a length of 10 mm. The cathode tube is constructed from graphite, boasting an outer diameter of 7 mm. At the inner front end of the cathode tube is a molybdenum orifice plate with a thickness of 0.5 mm and an orifice diameter of 2 mm.

Behind the emitter, there is a molybdenum spring. The primary purpose of this spring is to enhance the thermal resistance, reducing the cross-sectional area for heat conduction. To prevent any potential chemical reaction between the lanthanum hexaboride and refractory metals at elevated temperatures, graphite gaskets, each with a thickness of 0.5 mm and an inner diameter of 3 mm, are inserted between the emitter, molybdenum spring, and the molybdenum orifice plate.

Figure 4. Photograph of heaterless hollow cathode after 25 h of operation.

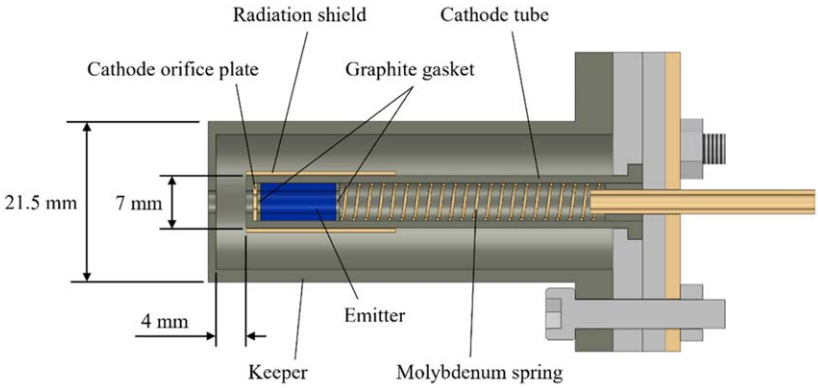

Figure 5. Cross-section of heaterless hollow cathode.

The front end of the cathode tube is enclosed with several loops of molybdenum foil, which serves as a radiation shield. This setup minimizes thermal energy loss from the cathode tube through radiation. The keeper, manufactured from graphite, has an inner diameter of 18 mm and an outer diameter of 21.5 mm. The distance from the keeper to the cathode tube is 4 mm. This specific spacing was determined based on achieving the Paschen minimum [57] at a flow rate of 40 sccm.

3.2. Experimental setup and procedure

The experiment was carried out in a vacuum chamber measuring 3 meters in length and 2 meters in diameter. Throughout the experiment, the background pressure of the chamber was consistently maintained within a range of 2 to 3×10^{-4} Torr. Apart from employing a larger vacuum chamber, the testing facilities are consistent with those described in the previous research [28]. Measurements of the primary discharge voltage and keeper voltage were acquired using a Teledyne LeCroy HDO4000A oscilloscope (1 GHz) paired with a Teledyne LeCroy PP020 voltage probe (500 MHz, 11 pF) and a Cybertek DP6700A high voltage differential probe (100 MHz, 5 pF), respectively.

Figure 6 illustrates the electrical connections employed in this research. During the experiment, the cathode tube, anode power supply, and keeper power supply were connected to the facility's common ground. Voltage probes, V_a and V_k, were utilized to measure the potentials of the anode and keeper, respectively. The discharge between the keeper and the emitter was initiated and sustained using a BK MR 100020 DC power supply (0–1000 V, 0–5 A). Meanwhile, the discharge between the anode and emitter was maintained by a BK MR50040 DC power supply (0–500 V, 0–10 A). All electrical circuits within the vacuum chamber were connected using Teflon-shielded wire to prevent disruptions from outgassing.

Figure 7 displays the argon gas pressure along the cathode's central axis during the three operational conditions and the ignition phase, as determined through analytic gas flow equations [13]. This pressure follows the modified Poiseuille law [58, 59], which is adapted for compressible gas [60].

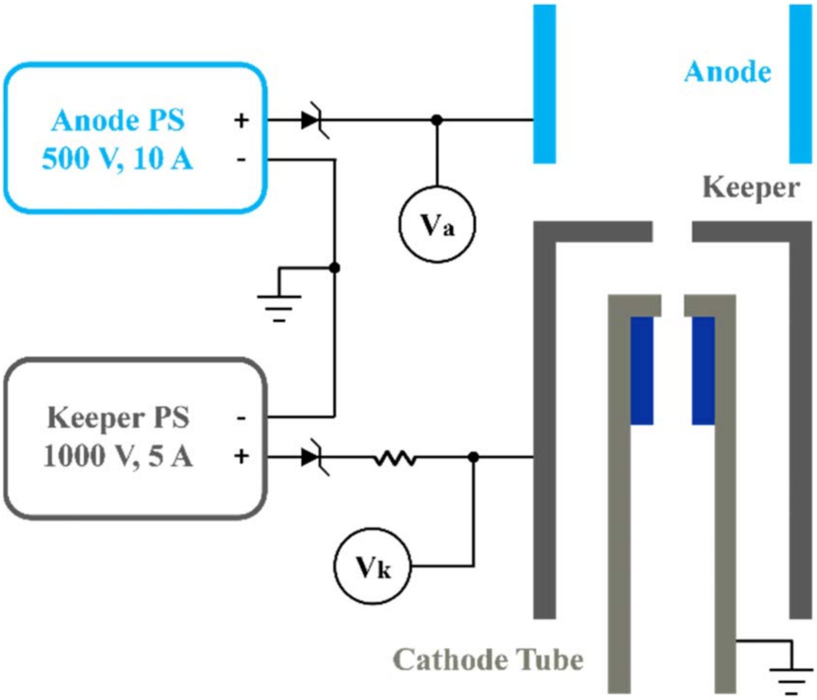

Figure 6. Electrical schematic for heaterless hollow cathode discharge.

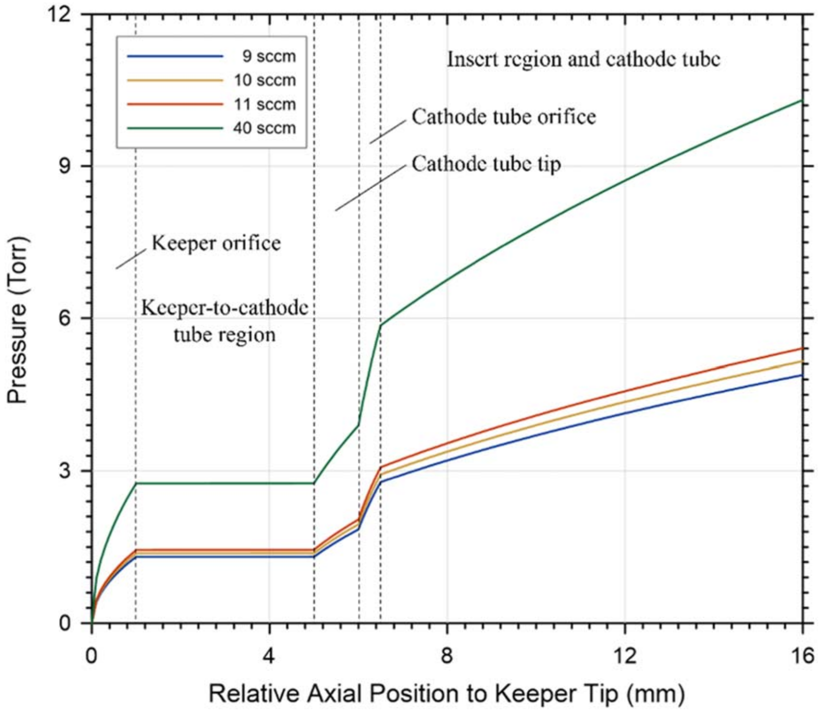

Figure 7. Neutral gas pressure during the three operational conditions and ignition phase.

The experimental procedure for the ignition and discharge of the heaterless hollow cathode is as follows:

1) Prior to the experiment, the cathode is purged with 50 sccm of argon for 15 min to clean the gas lines.

2) The gas flow rate is adjusted to 40 sccm, and a voltage of 900 V and a current of 1.8 A are applied to the keeper.

3) After the breakdown between the keeper and the cathode tube occurs, the flow rate is adjusted to 10 sccm.

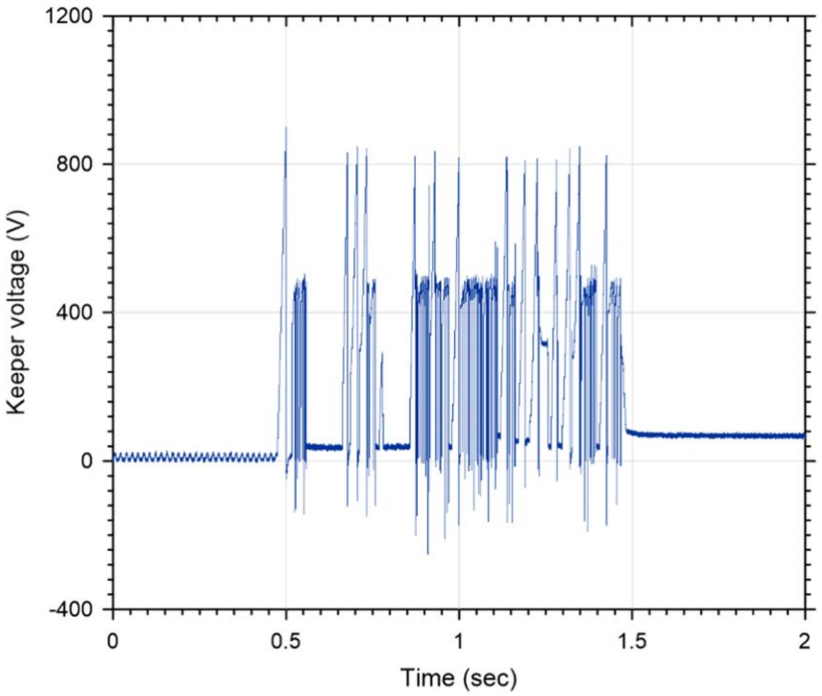

Figure 8. Keeper discharge voltage during the heating phase.

4) Once the keeper voltage decreases and stabilizes, the anode power supply is activated with 350 V and 2.5 A settings.
5) The keeper power supply is off after achieving a stable anode voltage, allowing diode mode operation.

The cathode is operated at the given flow rate and discharge current for 12 min before data capture on the oscilloscope to ensure that the emitter temperature has reached thermal equilibrium. If the cathode is exposed to atmospheric pressure between experiments, it is operated for 24 min before the experiment starts to maintain the emitter surface's condition. Figure 8 illustrates the keeper voltage recorded during the ignition and heating phases of the heaterless hollow cathode. Upon the voltage application to the keeper (as denoted in step 2), it is evident from the graph that a breakdown between the keeper and the cathode tube occurs at approximately an 850 V voltage difference. Following a brief period of about 1 second, characterized by notable oscillations in the keeper voltage (indicative of the heating process), the keeper voltage eventually stabilizes around 80 V.

4. Result and discussion

4.1. Influence of cylindrical anode surface roughness

The distance from the anode to the keeper was maintained at 50 mm while the cathode was discharging with the cylindrical anode. The coaxiality between the cathode and the cylindrical anode was also measured and adjusted to ensure it remained within a range of ±1 mm. Furthermore, prior to each experiment, the anode's surface was cleaned with alcohol to prevent the presence of non-conductive stains or coatings, which could influence the cathode's discharge characteristics. Figure 9 presents images of the cathode's discharge under operating conditions of 4 A discharge current and a flow rate of 11 sccm.

Figure 10 depicts the *I-V* curve of the heaterless hollow cathode discharge with different cylindrical anode surface roughness levels. Expressly, figures 10(a), (b), and (c) represent the discharge profiles of the hollow cathode at gas flow rates of 11 sccm, 10 sccm, and 9 sccm, respectively. Figure 10(a) shows that under a flow condition of 11 sccm and at a 4 A discharge current, the discharge voltage between the cathode and an anode with Ra 3.2 μm is 0.7 V lower than that of an anode with Ra 1.6 μm. Simultaneously, at the same discharge current, the discharge voltage between the cathode and Ra 6.4 μm anode is 2.0 V lower than that of Ra 3.2 μm anode. At a 6 A discharge current, the discharge voltage for the Ra 6.4 μm anode is 3.5 V and 2.5 V lower than those of the Ra 1.6 μm and Ra 3.2 μm anodes, respectively.

In figure 10(b), when the cathode operates at a flow rate of 10 sccm, the steady-state discharge voltage between the cathode and the Ra 3.2 μm anode is between 0.3 to 1.0 V lower than that of the Ra 1.6 μm anode.

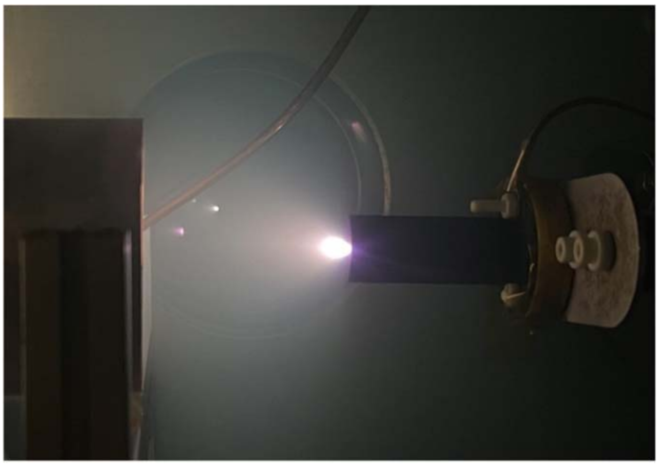

Figure 9. Photograph of heaterless hollow cathode discharge with cylindrical anode at the discharge current of 4 A and the flow rate of 11 sccm.

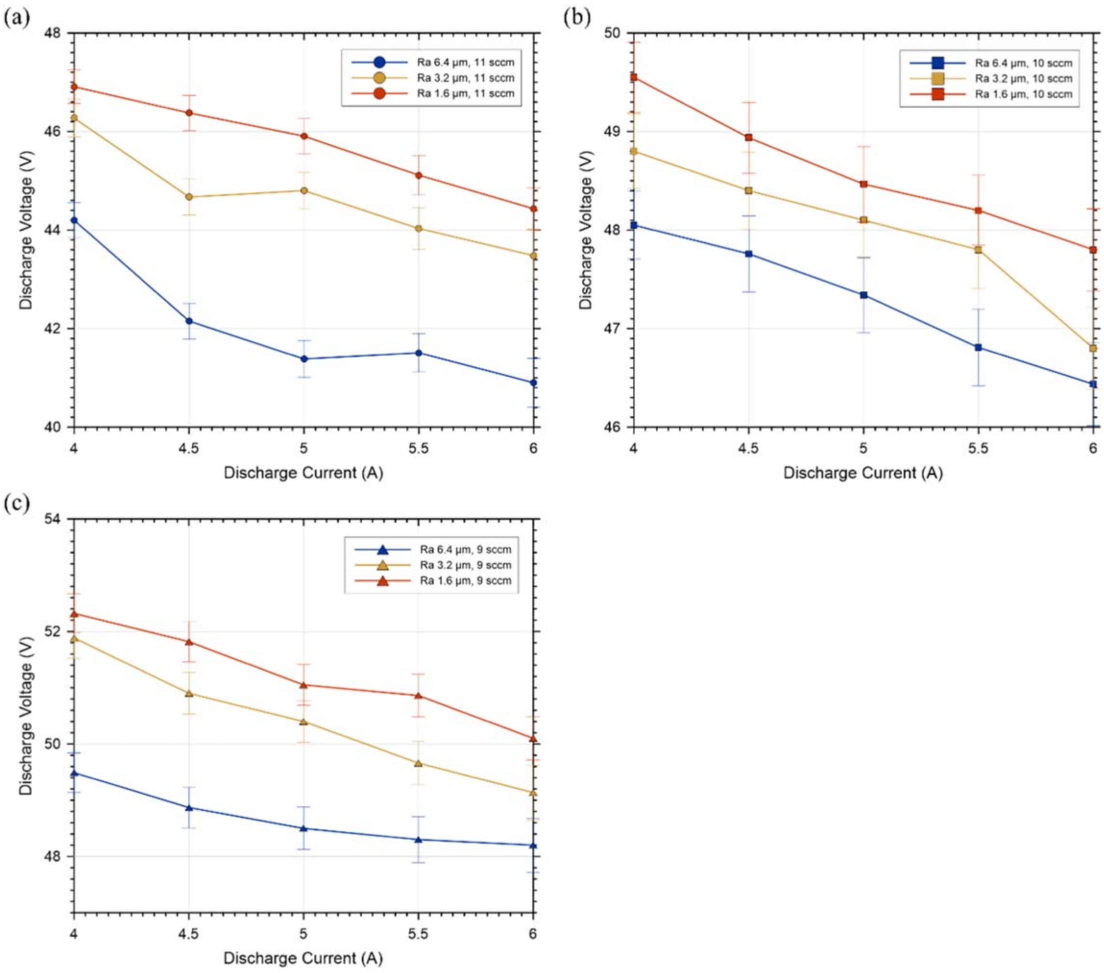

Figure 10. Plots of the *I*-*V* curve of the discharge with different cylindrical anode surface roughnesses at gas flow rates of (a) 11 sccm, (b) 10 sccm, and (c) 9 sccm.

Meanwhile, the discharge voltage with the Ra 6.4 μm anode is between 0.4 to 1.0 V lower than that of the Ra 3.2 μm anode. A similar trend, where the Ra value is inversely proportional to the discharge voltage, can also be observed in figure 10(c).

The negative correlation between anode roughness and discharge voltage (i.e., the discharge voltage with the Ra 6.4 μm anode is the lowest) can be attributed to the surface area of the anode. The internal surface area of the

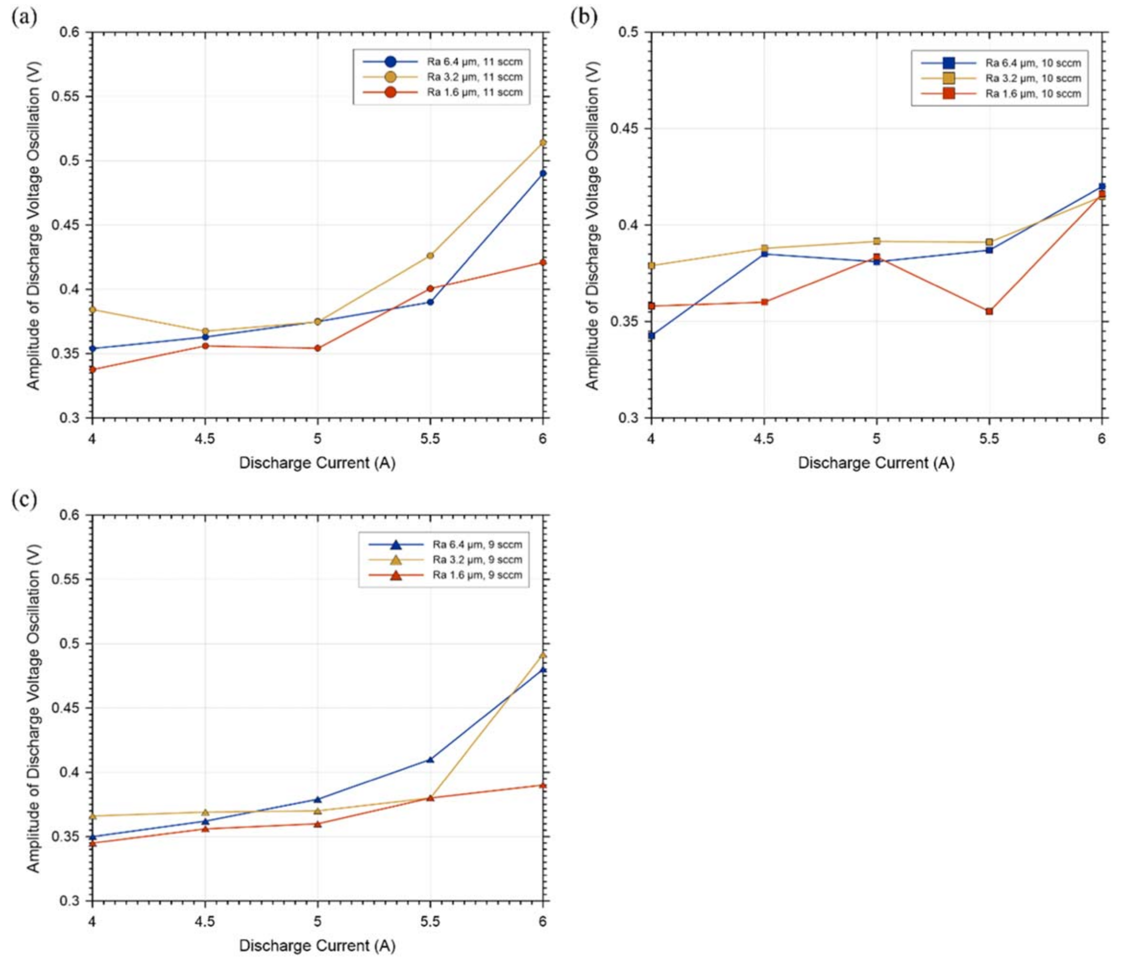

Figure 11. Plots of the amplitude of discharge voltage oscillations with different cylindrical anode surface roughnesses at gas flow rates of (a) 11 sccm, (b) 10 sccm, and (c) 9 sccm.

cylindrical anode under different surface roughness conditions is illustrated in figure 3. According to the calculation results, an increase in the Ra value leads to an expansion in the anode's surface area. Given identical length and diameter, an anode with a larger surface area implies a potential reduction in the discharge voltage needed to sustain the same discharge current.

Two additional trends can be discerned from figure 10. Firstly, there is an inverse relationship between the cathode discharge voltage and the discharge current, consistent with previous findings [28], and can be explained by a decrease in the emitter sheath voltage [61]. As the electron energy flux delivered to the emitter surface rises, it consequently elevates the temperature of the emitter surface, thereby enhancing the density of the thermionic emission current and reducing the requisite discharge voltage.

The second general trend discernible from figure 10 is that the discharge current is inversely proportional to the gas flow rate. This observation can be attributed to increased emitter temperature during operation. As the gas flow rate augments, the plasma drift resistance in the cathode tube orifice also escalates [13]. As plasma traverses through the high-resistance cathode tube orifice, the cathode plasma experiences heightened resistance, leading to increased collisions among charged particles. This results in pronounced resistive heating in the orifice plasma. The resulting ohmic power is convectively transferred to the orifice plate due to plasma bombardment, which heats the cathode tube and emitter via conduction and radiation.

Figure 11 displays the amplitude of discharge current oscillations when the cathode operates under different flow rates and in conjunction with different anodes. Expressly, figures 11(a), (b), and (c) represent the cathode operating under flow rates of 11 sccm, 10 sccm, and 9 sccm, respectively. Various factors, including the physical characteristics of the anode, the specific flow rate, and other operating conditions, can influence the oscillations in the discharge voltage. The definition of the discharge voltage oscillation amplitude Δ in this study is as follows [62]:

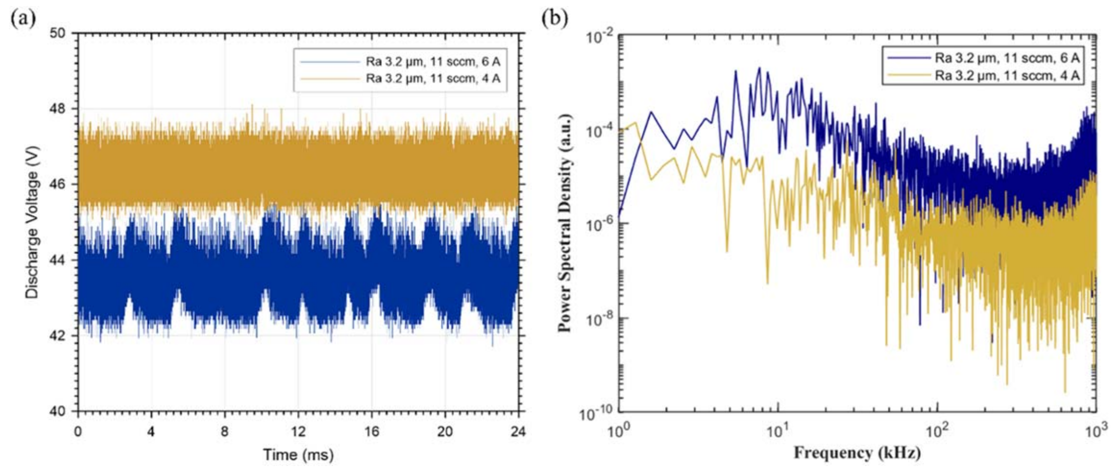

Figure 12. (a) Time-varying waveforms and (b) power spectral density at the discharge current of 6 A and 4 A with the gas flow rate of 11 sccm.

$$\Delta = \sqrt{\frac{\int_0^{\tau} (V_a - \overline{V}_a)^2 dt}{\tau}}, \tag{2}$$

where τ denotes the measurement time, V_a denotes the discharge voltage, and $\overline{V}_a$ denotes the average discharge voltage. The amplitude of the discharge voltage oscillation is measured as the standard deviation of the discharge voltage. This measurement method aligns with approaches from other research, particularly those evaluating discharge current in Hall thrusters [62, 63].

It can be observed from figure 11 that the surface roughness of the cylindrical anode does not seem to have a direct correlation with the discharge voltage oscillations. When the cathode discharges with anodes of Ra 6.4 μm, Ra 3.2 μm, and Ra 1.6 μm, the discharge voltage oscillation remains relatively similar, all less than 0.6 V. Another discernible trend in figure 11 indicates that as the discharge current increases, there is a slight rise in discharge voltage oscillations, which can be attributed to the intensification of ionization-like instabilities and IAT [64].

Hollow cathode discharge oscillation can be classified into three categories based on frequency [16, 35]. The first category encompasses oscillations induced by the power supply, typically exhibiting frequencies below 1 kHz [35]. The second type is characterized by large-scale ionization-like oscillations, with frequencies ranging from 10 to 150 kHz [16]. These oscillations often exhibit large-scale fluctuations in plasma density and discharge current. Recent studies have harnessed high-speed imaging techniques, serving as non-intrusive diagnostic tools, to capture these ionization-like oscillations directly within the cathode plume [64]. The third type pertains to IAT, encompassing broadband, turbulent fluctuations with frequencies surpassing 200 kHz [16]. IAT represents an electrostatic plasma instability, intensifying due to the pronounced electron drift observed when a substantial difference exists between ion and electron temperatures coupled with a high electron drift velocity [65–67]. The latest advancements in modeling and experimentation concerning hollow cathodes have demonstrated that the onset of IAT under elevated discharge current or diminished mass flow rate can trigger coherent ionization-like instabilities [68–70].

Figures 12(a) and (b) depict the temporal waveforms and PSD analysis when the cathode operates at a discharge current of 6 A and 4 A with a flow rate of 11 sccm and in conjunction with a Ra 3.2 μm anode, respectively. The PSD examination in figure 12(b) identifies low-frequency oscillations ranging from 10 to 150 kHz and broadband perturbations exceeding 200 kHz, indicating the amplified presence of ionization-like instabilities and IAT within the cathode plume when operating under a high discharge current regime.

4.2. Influence of planar anode surface roughness influence

Analogous to the cylindrical anode's mounting methodology, the planar anode's placement in these experiments maintains a fixed distance of 50 mm from the cathode. Before initiating each experimental setup, the anode's surface undergoes a thorough cleaning process to ensure the accuracy of the results. Figures 13(a), (b), and (c) present the *I-V* curves for the heaterless hollow cathode operating with planar anodes of varying surface roughnesses under the flow rate conditions of 11 sccm, 10 sccm, and 9 sccm, respectively.

Several key observations can be discerned from figure 13. Firstly, there is an inverse relationship between the discharge voltage and the discharge current, indicating that as the discharge current rises, the discharge voltage drops. Secondly, the discharge voltage shows a distinct negative correlation with the surface roughness of the

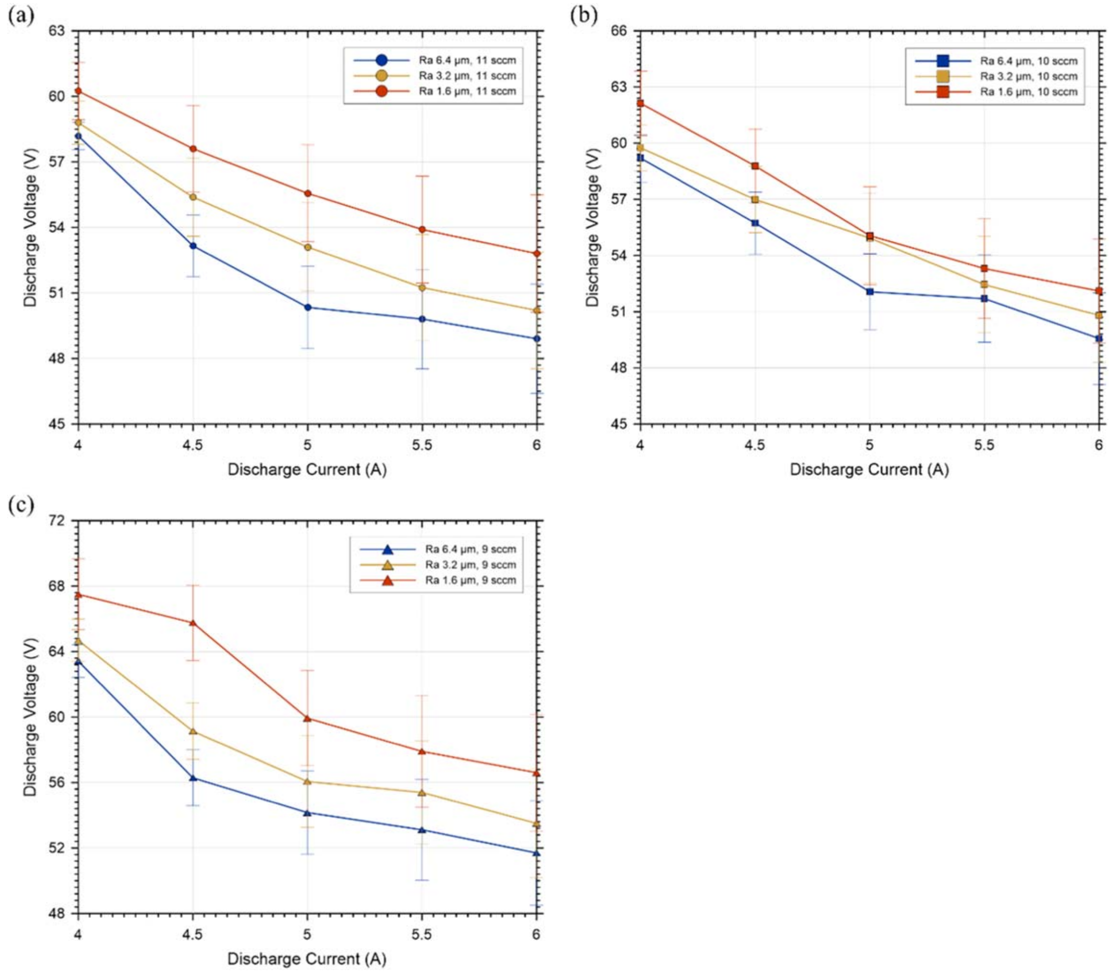

Figure 13. Plots of the *I*-*V* curve of the discharge with different planar anode surface roughnesses at gas flow rates of (a) 11 sccm, (b) 10 sccm, and (c) 9 sccm.

planar anode. In particular, when the cathode is paired with an anode characterized by a Ra value of 6.4 μm, the required discharge voltage is notably lower than when combined with anode Ra values of 3.2 μm and 1.6 μm. Moreover, as the discharge current increases, discharge voltage oscillations are amplified. Lastly, the Ra value of the planar anode appears to influence these voltage oscillations, with a rougher anode surface seemingly suppressing plasma oscillations within the cathode plume.

The negative resistance observed in figure 13 can be attributed to the augmented electron energy flux directed towards the emitter surface. This enhancement reduces the necessary discharge voltage to extract sufficient thermionic electrons, ensuring the anode power supply remains in its control current mode. The increased surface area can elucidate the relationship between the discharge voltage and the roughness of the anode surface. As demonstrated in figure 3, the surface area of the planar anode under different roughness conditions indicates that the anode surface area at a Ra 6.4 μm roughness is approximately 1.5 times larger than that of the anode at a Ra 1.6 μm roughness. This enhanced surface area aids the anode in lowering the required discharge voltage needed to sustain the primary discharge.

Figure 14 elucidates the influence of anode surface roughness and gas flow rate on discharge voltage oscillation. At a flow rate of 11 sccm, when the cathode discharges with planar anodes of Ra 6.4 μm, Ra 3.2 μm, and Ra 1.6 μm, the oscillations in the discharge voltage at a discharge current of 6 A surpass those at 4 A by 1.9 V, 1.7 V, and 1.4 V, respectively. A similar trend is observed when the hollow cathode gas flow rate is set at 10 sccm and 9 sccm. Broadly, the discharge voltage oscillation directly correlates with the hollow cathode's discharge current, possibly due to the amplification of ionization-like instabilities and IAT when the cathode operates in a high discharge current regime. This phenomenon is frequently characterized as the plume mode operation of the hollow cathode. The operational state of the hollow cathode is commonly categorized into spot mode and plume mode based on its discharge profile [71–73]. The spot mode represents a relatively quiescent and stable discharge mode, while the plume mode is a precarious mode in which the anode voltage or current typically

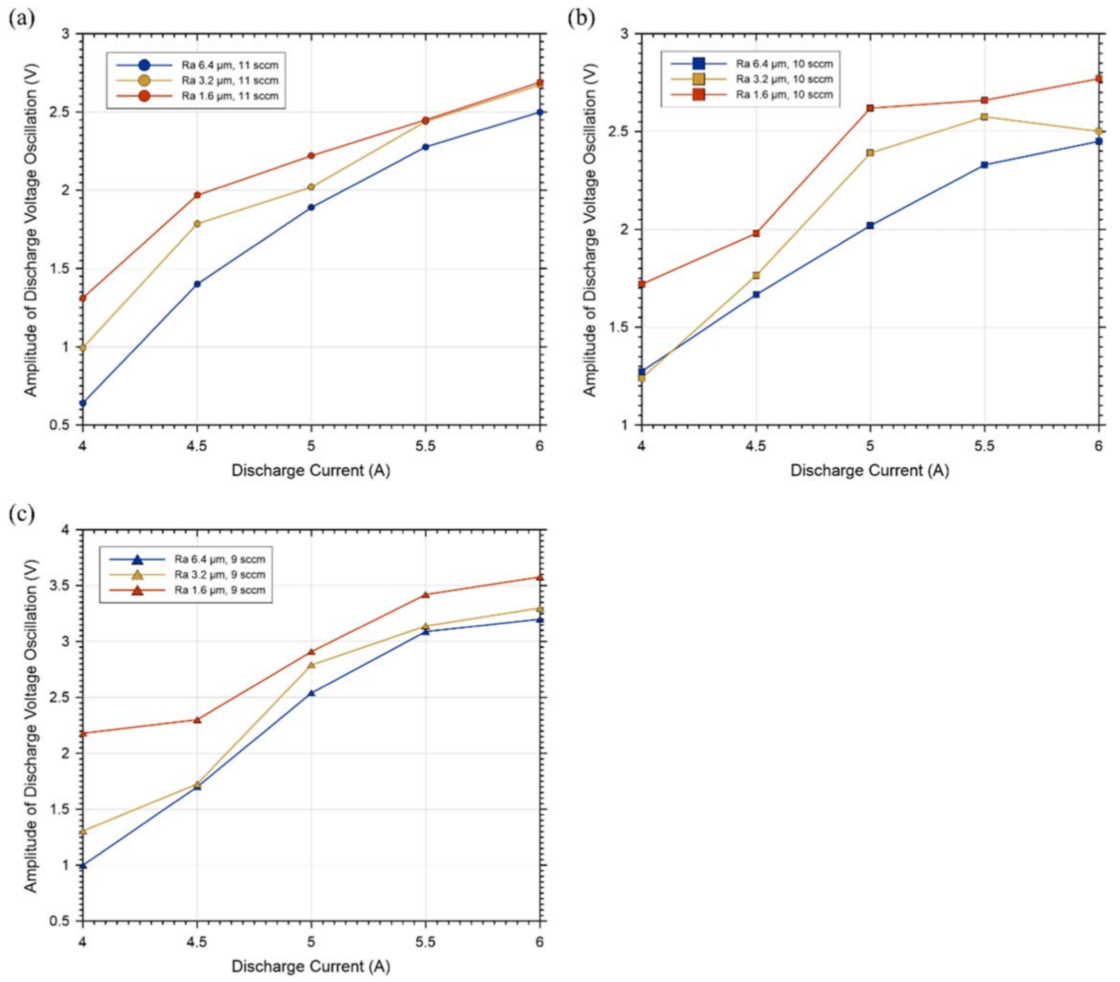

Figure 14. Plots of the amplitude of discharge voltage oscillations with different planar anode surface roughnesses at gas flow rates of (a) 11 sccm, (b) 10 sccm, and (c) 9 sccm.

experiences intense oscillations. Moreover, wear on the cathode orifice plate is accelerated in the plume mode due to the heightened production of energetic ions in the plume region [35].

Figure 14 further illustrates that the surface roughness of the planar anode appears to influence the discharge voltage oscillation. At 11 sccm, 10 sccm, and 9 sccm flow rates, the cathode discharging with a Ra 1.6 μm anode consistently exhibits the highest voltage oscillations, followed by discharges with a Ra 3.2 μm anode. Conversely, voltage oscillations are invariably the lowest when the cathode discharges with a Ra 6.4 μm anode. This observation suggests that a rougher surface on the planar anode might suppress the ionization-like instabilities and IAT within the cathode plume. To delve deeper into this phenomenon, a PSD analysis of cathode operation with anodes of varying surface roughness under identical operating conditions has been conducted and is presented in figure 15.

Figure 15 shows that ionization instabilities and IAT are most pronounced when the anode surface roughness is at Ra 1.6 μm. Conversely, when the surface roughness is at Ra 6.4 μm, these phenomena are the most suppressed, with the Ra 3.2 μm anode lying between the two extremes. One potential reason this phenomenon is observed with the planar anode but not with the cylindrical anode might relate to the direction of neutral gas diffusing from the cathode and the neutral gas density on the anode surface. Some studies have found that the plasma potential oscillation in the hollow cathode discharge, triggered by ionization instabilities or IAT in the cathode plume region, can be mitigated by injecting neutral gas directly into the cathode plume region via an external gas feed [74, 75].

Figure 16 provides a schematic representation of the neutral gas flow during cathode discharge. During the discharge process between the cathode and planar anode, some non-ionized neutral gas flows toward the surface of the planar anode. This gas then diffuses around the planar anode, driven by the surface's pressure gradient and plasma bombardment. As a result of the extended contact time and path between the neutral gas particles and the surface of the planar anode, the surface roughness of the planar anode slightly influences the velocity of these particles, indirectly affecting the neutral gas density and gradient on the anode surface and between the anode

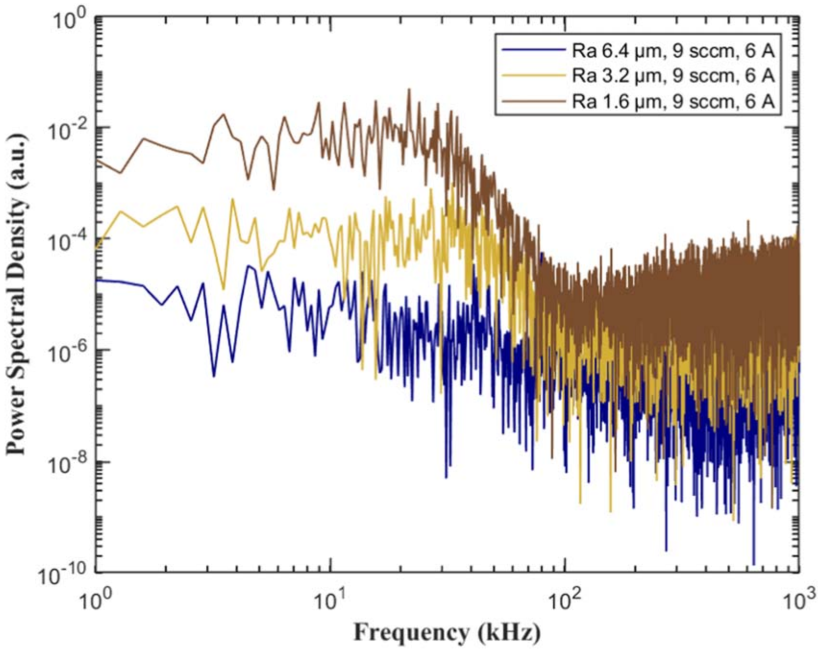

Figure 15. Power spectral density at the discharge current of 6 A at the flow rate of 9 sccm with different surface roughnesses.

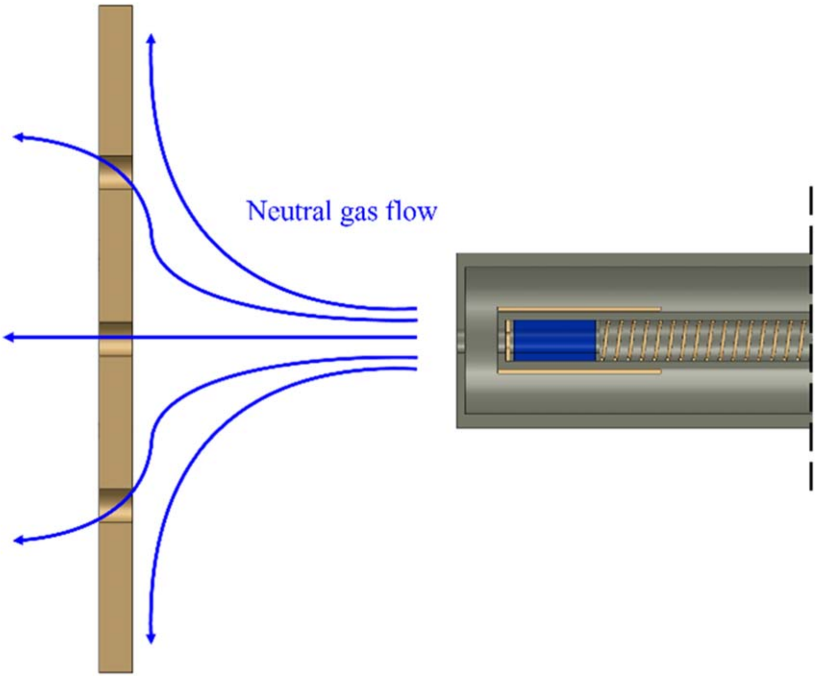

Figure 16. Schematic of the neutral gas flow direction during the cathode discharge.

and cathode. The reason why the surface roughness of the cylindrical anode has a less significant impact on its discharge voltage oscillations might be that, during discharge between the cathode and cylindrical anode, neutral gas exiting the cathode can directly traverse the center of the anode, reaching the vacuum chamber walls, reduces the contact path and probability between the neutral gas particles and the surface of the cylindrical anode, subsequently diminishing the influence of the cylindrical anode's surface roughness on its discharge voltage oscillations.

5. Conclusion

The exploration of heaterless hollow cathode discharges concerning planar and cylindrical anode surface roughness, as presented in this research, has elucidated several phenomena central to the operation of such devices. One of the findings is the prominent correlation between discharge voltage and anode surface roughness. As the anode surface roughness increases, the required discharge voltage decreases in cylindrical and planar anodes, suggesting that a more pronounced roughness potentially provides an enhanced surface area that facilitates more electron current collection, thereby decreasing the necessary discharge voltage to sustain the primary discharge.

Further compounding this relationship is observing a negative resistance in the discharge and the increased plasma instabilities within the cathode plume, the former potentially owing to the increased electron energy flux to the emitter while the latter can be attributed to the enhanced ionization-like instabilities and IAT during high current discharge.

A key observation from the data is how anode surface roughness impacts ionization-like instabilities and IAT within the cathode plume. These instabilities become particularly evident in planar anodes with a surface roughness of Ra 1.6 μm. Conversely, anodes characterized by roughness of Ra 6.4 μm reduced these instabilities, suggesting that rougher surfaces might alleviate adverse effects within cathode plumes. This behavior diverges when examining cylindrical anodes. Unlike planar counterparts, the discharge voltage oscillations of cylindrical anodes appear less influenced by their surface roughness. The neutral gas flow dynamics, particularly its direct traverse through the anode center, reduce the influence of surface roughness on discharge behaviors.

Ultimately, these findings illuminate the interplay between anode surface roughness and hollow cathode discharges. Understanding these dynamics can guide design choices in systems dependent on such cathodes, ensuring enhanced efficiency and extended operational life. Future studies will delve deeper into this area, employing intrusive measurement probes and high-speed cameras to investigate the influence of anode surface roughness on cathode plasma characteristics in the cathode plume region, including aspects like plasma potential, electron and ion temperatures, and plume instabilities.

Acknowledgments

Financial support for this work was provided by the National Science and Technology Council and Ministry of Science and Technology (Taiwan) under grant numbers NSTC 112-2628-E-006-005-MY3, NSTC 112-2218-E-006-015, MOST 108-2628-E-006-008-MY3.

Data availability statement

All data that support the findings of this study are included within the article (and any supplementary files).

ORCID iDs

Jordan H Hsieh https://orcid.org/0000-0001-8120-2744
Heri Juwantono https://orcid.org/0000-0002-1450-0052
Yueh-Heng Li https://orcid.org/0000-0001-9129-2747

References

[1] Choueiri E Y 2004 A critical history of electric propulsion: The first 50 years (1906-1956) *J. Propul. Power* **20** 193–203

[2] Sovey J S, Rawlin V K and Patterson M J 2001 Ion propulsion development projects in US: Space electric rocket test I to deep space 1 *J. Propul. Power* **17** 517–26

[3] Rivkin A S and Cheng A F 2023 Planetary defense with the double asteroid redirection test (DART) mission and prospects *Nat. Commun.* **14** 1003

[4] Li Y-H, Pan J-Y and Herdrich G 2020 Design and demonstration of micro-scale vacuum cathode arc thruster with inductive energy storage circuit *Acta Astronaut.* **172** 33–46

[5] Li Y-H, Palagiri S, Chang P-Y, Montag C and Herdrich G 2019 Plasma behavior in a solid-fed pulsed plasma thruster *Journal of Aeronautics, Astronautics and Aviation* **51** 31–42

[6] Li Y-H, Dorn K, Hsieh H-C, Kuo T-C and Hsu Y-C 2021 Effect of electrode angle on pulsed plasma thruster performance *Journal of Aeronautics, Astronautics and Aviation* **53** 353–67

[7] Li Y-H, Huang T-Y, Shen M M and Chen Y-C 2023 Development of miniature radio frequency ion thruster with inductively coupled plasma source *Journal of Aeronautics, Astronautics and Aviation* **55** 13–28

[8] Li Y-H, Chen Y-C, Liu S-W and Aslan A R 2023 Prediction and optimization of thrust performance from plasma diagnostics in the inductively coupled plasma of an RF ion thruster *Acta Astronaut.* **208** 130–141

[9] Hsieh J H, Li Y-H, Shen M M and Lien W-C 2022 Hectowatt-class double-peaked hall thruster for future space missions *International Electric Propulsion Conference 2022 (Boston, MA, USA, June 19-23)*
[10] Boeuf J-P 2017 Tutorial: physics and modeling of hall thrusters *J. Appl. Phys.* **121** 011101
[11] Conversano R W, Goebel D M, Hofer R R, Mikellides I G and Wirz R E 2017 Performance analysis of a low-power magnetically shielded hall thruster: Experiments *J. Propul. Power* **33** 975–83
[12] Vaudolon J, Mazouffre S, Hénaux C, Harribey D and Rossi A 2015 Optimization of a wall-less hall thruster *Appl. Phys. Lett.* **107** 174103
[13] Goebel D M and Katz I 2008 *Fundamentals of Electric Propulsion: Ion and Hall thrusters* (New York: Wiley)
[14] Hsieh J H and Li Y-H 2023 Review of hollow cathode discharge: exploring advanced design and optimization *Journal of Aeronautics, Astronautics and Aviation* **55** 385–413
[15] Dushman S 1923 Electron emission from metals as a function of temperature *Phys. Rev.* **21** 623
[16] Lev D R, Mikellides I G, Pedrini D, Goebel D M, Jorns B A and McDonald M S 2019 Recent progress in research and development of hollow cathodes for electric propulsion *Reviews of Modern Plasma Physics* **3** 1–89
[17] Tian F, Miao L, Xia Q, Liang F, Wang N and Hou X 2023 Analysis of the effect of keeper working conditions on hollow cathode performance *Acta Astronaut.* **211** 130–141
[18] Liu C, Ning Z, Zhu X and Yu D 2023 The influence of keeper current on the performance of magnetically enhanced hollow cathode thruster *Vacuum* **215** 112339
[19] Kirkwood D M, Gross S J, Balk T J, Beck M J, Booske J, Busbaher D, Jacobs R, Kordesch M E, Mitsdarffer B and Morgan D 2018 Frontiers in thermionic cathode research *IEEE Trans. Electron Devices* **65** 2061–71
[20] Cronin J L 1979 Practical aspects of modern dispenser cathodes *Microwave Journal* **22** 57–62
[21] Becatti G and Goebel D M 2022 500-A LaB6 hollow cathode for high power electric thrusters *Vacuum* **198** 110895
[22] Payman A R and Goebel D M 2022 Development of a 50-A heaterless hollow cathode for electric thrusters *Rev. Sci. Instrum.* **93** 113543
[23] Goebel D M and Payman A R 2023 Heaterless 300 a lanthanum hexaboride hollow cathode *Rev. Sci. Instrum.* **94** 033506
[24] Rand L, Qian X and Williams J 2010 Ultra low work function, non-consumable insert for hollow cathodes formed from C12A7 electride *57th JANNAF Propulsion Meeting* in
[25] Rand L P, Waggoner R M and Williams J D 2011 Hollow cathode with low work function electride insert *ASME International Mechanical Engineering Congress and Exposition (Denver, Colorado, USA, November 11–17)* 317–323 inIMECE2011-65785
[26] Dan G B and Goebel M 2022 High current hollow cathodes for high power electric thrusters(IEPC paper) 2022–101
[27] Goebel D M, Watkins R M and Jameson K K 2007 LaB6 hollow cathodes for ion and hall thrusters *J. Propul. Power* **23** 552–8
[28] Hsieh J H, Shen M M, Li Y-H and Huang P-H 2023 Development of a lanthanum hexaboride hollow cathode for a magnetic octupole thruster *Vacuum* **214** 112146
[29] Becatti G, Conversano R W and Goebel D M 2021 Demonstration of 25,000 ignitions on a proto-flight compact heaterless lanthanum hexaboride hollow cathode *Acta Astronaut.* **178** 181–91
[30] Lev D and Appel L 2016 Heaterless hollow cathode technology - a critical review *5th Space Propulsion Conference (Rome, Italy, 2–6 May 2016)* inSP2016 3125366
[31] Suzuki A, Kinefuchi K, Ichihara D, Cho S, Watanabe H and Kubota K 2023 Energetic ion and plasma oscillation measurements during plume mode operation of a hollow cathode *Phys. Plasmas* **30**
[32] Goebel D M and Watkins R M 2010 Compact lanthanum hexaboride hollow cathode *Rev. Sci. Instrum.* **81** 083504
[33] Vekselman V, Krasik Y E, Gleizer S, Gurovich V T, Warshavsky A and Rabinovich L 2013 Characterization of a heaterless hollow cathode *J. Propul. Power* **29** 475–86
[34] Eichhorn H, Schoenbach K and Tessnow T 1993 Paschen's law for a hollow cathode discharge *Appl. Phys. Lett.* **63** 2481–3
[35] Goebel D M, Becatti G, Mikellides I G and Lopez Ortega A 2021 Plasma hollow cathodes *J. Appl. Phys.* **130** 050902
[36] Conversano R W, Becatti G, Goebel D M and Chaplin V H 2022 Demonstration of 13,011-h of operation of a proto-flight compact heaterless lanthanum hexaboride hollow cathode *Acta Astronaut.* **197** 53–9
[37] Potrivitu G-C, Joussot R and Mazouffre S 2018 Anode position influence on discharge modes of a LaB6 cathode in diode configuration *Vacuum* **151** 122–32
[38] Csiky G A 1969 Measurements of some properties of a discharge from a hollow cathode *NASA Technical Note* D-4966
[39] Potrivitu G-C, Mazouffre S, Grimaud L and Joussot R 2019 Anode geometry influence on LaB6 cathode discharge characteristics *Phys. Plasmas* **26** 113506
[40] Jameson K K, Goebel D M and Watkins R M 2005 Hollow cathode and thruster discharge chamber plasma measurements in*29th Int. Electric Propulsion Conf.*
[41] Farnell C C, Williams J D and Farnell C C 2011 Comparison of hollow cathode discharge plasma configurations *Plasma Sources Sci. Technol.* **20** 025006
[42] Qin Y, Xie K and Ouyang J 2017 Measurements and analysis of potential oscillations near the hollow cathode *Procedia engineering* **185** 17–23
[43] Zhou Y, Zhu H, Zhang W, Zuo X, Li Y and Yang J 2015 Influence of surface roughness on the friction property of textured surface *Advances in Mechanical Engineering* **7** 1687814014568500
[44] Whitehouse D J 2002 *Surfaces and Their Measurement* (Boca Raton, FL: CRC Press)
[45] Joussot R, Grimaud L and Mazouffre S 2017 Examination of a 5 A-class cathode with a LaB6 flat disk emitter in the 2 A–20 A current range *Vacuum* **146** 52–62
[46] Coletti M and Gabriel S 2012 Insert temperature measurements of a 180A hollow cathode for the HiPER project in*48th AIAA/ASME/SAE/ASEE Joint Propulsion Conf. & Exhibit* 4081
[47] Brophy J and Garner C 1988 Tests of high current hollow cathodes for ion engines in*24th Joint Propulsion Conf.* 2913
[48] Brophy J and Garner C 1991 A 5,000 h xenon hollow cathode life test in*27th Joint Propulsion Conf.* 2122
[49] Kamhawi H and Van J 2012 Noord, Development and testing of high current hollow cathodes for high power hall thrusters in*48th AIAA/ASME/SAE/ASEE Joint Propulsion Conf. & Exhibit* 4080
[50] Puchkov P M 2017 The low-current cathode for a small power electric propulsion in*7th European Conference for Aeronautics and Space Sciences* 3–6
[51] Goebel D M and Polk J E 2016 Lanthanum hexaboride hollow cathode performance and wear testing for the asteroid redirect mission Hall thruster in*52nd AIAA/SAE/ASEE Joint Propulsion Conf.* 4835
[52] Oshio Y, Kubota K, Watanabe H, Cho S, Ohkawa Y and Funaki I 2019 Experimental investigation of LaB6 hollow cathode with radiative heater *Transactions Of The Japan Society For Aeronautical And Space Sciences, Aerospace Technology Japa.* **17** 203–10
[53] Ning Z-X, Zhang H-G, Zhu X-M, Ouyang L, Liu X-Y, Jiang B-H and Yu D-R 2019 10000-ignition-cycle investigation of a LaB 6 hollow cathode for 3–5-kilowatt hall thruster *J. Propul. Power* **35** 87–93

[54] Drobny C, Tajmar M and Wirz R 2017 Development of a C12A7 electride hollow cathode in*35th Int. Electric Propulsion Conf.* 1–8

[55] Chu E and Goebel D M 2012 High-current lanthanum hexaboride hollow cathode for 10-to-50-kW Hall thrusters *IEEE Trans. Plasma Sci.* **40** 2133–44

[56] Lev D, Alon G, Appel L, Seeman O and Hadas Y 2017 Low current heaterless hollow cathode development overview in*35th Int. Electric Propulsion Conf.*

[57] Paschen F 1889 Ueber die zum funkenübergang in luft: wasserstoff und kohlensäure bei verschiedenen drucken erforderliche potentialdifferenz *JA Barth* **273** (5) 69–96

[58] Dushman S 1962 *Scientific Foundations of Vacuum Technique* (New York: Wiley)

[59] Herzfeld K F and Smallwood H M 1931 *Taylor's Treatise on Physical Chemistry* 2nd ed. (D. Van Nostrand Co.)

[60] Roth A 2012 *Vacuum Technology* (Amsterdam: Elsevier)

[61] Riccardo A, Mariano A, Pedrini D and Paganucci F 2013 Preliminary characterization of a LaB6 hollow cathode for low-power hall effect thrusters in*33rd Int. Electric Propulsion Conf.*

[62] Watanabe H, Cho S and Kubota K 2020 Performance and plume characteristics of an 85 W class hall thruster *Acta Astronaut.* **166** 227–37

[63] Yamamoto N, Komurasaki K and Arakawa Y 2005 Discharge current oscillation in Hall thrusters *J. Propul. Power* **21** 870–6

[64] Georgin M 2020 *Ionization instability of the hollow cathode plume* University of Michigan in

[65] Potrivitu G-C and Xu S 2022 Evidence of the ionization instability and ion acoustic turbulence correlation in sub-ampere hollow cathodes *Journal of Electric Propulsion* **1** 1–22

[66] Jorns B A, Mikellides I G and Goebel D M 2014 Ion acoustic turbulence in a 100-A LaB 6 hollow cathode *Phys. Rev.* E **90** 063106

[67] Georgin M P, Jorns B A and Gallimore A D 2017 An experimental and theoretical study of hollow cathode plume mode oscillations *Int. Electric Propulsion Conf.* IEPC-2017

[68] Sary G, Garrigues L and Boeuf J-P 2017 Hollow cathode modeling: II. physical analysis and parametric study *Plasma Sources Sci. Technol.* **26** 055008

[69] Sary G, Garrigues L and Boeuf J-P 2017 Hollow cathode modeling: I. a coupled plasma thermal two-dimensional model *Plasma Sources Sci. Technol.* **26** 055007

[70] Georgin B A J M P and Gallimore A D 2019 Onset criterion for a turbulence-driven ionization instability in hollow cathodes(IEPC paper) IEPC- 2019-2155

[71] Rawlin V K and Pawlik E V 1968 A Mercury plasma-bridge neutralizer *J. Spacecr. Rockets* **5** 814-820

[72] Csiky G A 1969 Investigation of a hollow cathode discharge plasma *Inst. of Aeronautics and Astronautics, Electric Propulsion Conference* (American Inst. Of Aeronautics and Astronautics)

[73] Siegfried D and Wilbur P 1978 An investigation of mercury hollow cathode phenomena *13th Int. Electric Propulsion Conf.* 705 in

[74] Goebel D M, Jameson K K, Katz I and Mikellides I G 2007 Plasma potential behavior and plume mode transitions in hollow cathode discharges *Electric Propulsion Conference* (IEPC paper)

[75] Goebel D M, Jameson K K, Katz I and Mikellides I G 2007 Potential fluctuations and energetic ion production in hollow cathode discharges *Phys. Plasmas* **14** 103508